Science of the Total Environment 920 (2024) 170931

Contents lists available at ScienceDirect

Science of the Total Environment

journal homepage: www.elsevier.com/locate/scitotenv

Degradation of ice-wedge polygons leads to increased fluxes of water and DOC

Niek Jesse Speetjens [a,b,*], Wouter R. Berghuijs [a], Julia Wagner [c], Jorien E. Vonk [a]

[a] Department of Earth Sciences, Vrije Universiteit Amsterdam, 1081 HV Amsterdam, the Netherlands
[b] School of Environmental Studies (ENVI), University of Victoria, V8W 2Y2 Victoria, BC, Canada
[c] Department of Physical Geography, Stockholm University (SU), 106 91 Stockholm, Sweden

HIGHLIGHTS

- More, seasonal runoff in degraded ice-wedge polygon systems under climate warming
- More baseflow dominated runoff mobilizes larger proportions of soil carbon stocks
- Longer season drives increased flux, concentration remains unchanged
- Parsimonious hydro-biogeochemical models provide scalable micro-to-macro solution

GRAPHICAL ABSTRACT

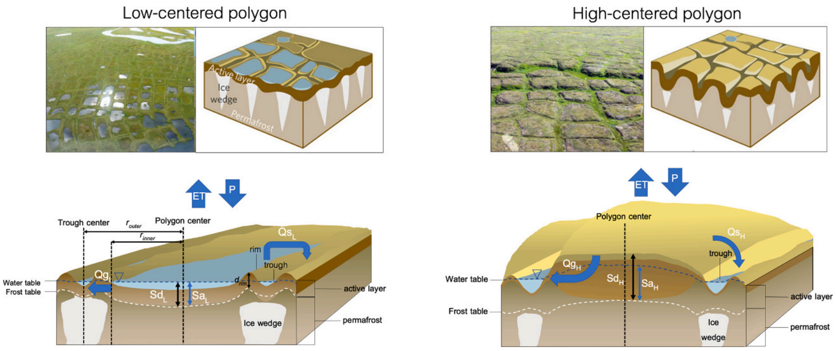

ARTICLE INFO

Editor: Christian Herrera

Keywords:
Permafrost
Hydrology
Ice-wedge polygon
Lateral carbon flux
Model
Dissolved organic carbon

ABSTRACT

Ice-wedge polygon landscapes make up a substantial part of high-latitude permafrost landscapes. The hydrological conditions shape how these landscapes store and release organic carbon. However, their coupled water-carbon dynamics are poorly understood as field measurements are sparse in smaller catchments and coupled hydrology-dissolved organic carbon (DOC) models are not tailored for these landscapes. Here we present a model that simulates the hydrology and associated DOC export of high-centered and low-centered ice-wedge polygons and apply the model to a small catchment with abundant polygon coverage along the Yukon Coast, Canada. The modeled seasonal pattern of water and carbon fluxes aligns with sparse field data. These modeled seasonal patterns indicate that early-season runoff is mostly surficial and generated by low-centered polygons and snow trapped in troughs of high-centered polygons. High-centered polygons show potential for deeper subsurface flow under future climate conditions. This suggests that high-centered polygons will be responsible for an increasing proportion of annual DOC export compared to low-centered polygons. Warming likely shifts low-centered polygons to high-centered polygons, and our model shows that this shift will cause a deepening of the active layer and a lengthening of the thawing season. This, in turn, intensifies seasonal runoff and DOC flux, mainly through its duration. Our model provides a physical hypothesis that can be used to further quantify and refine our understanding of hydrology and DOC export of arctic ice-wedge polygon terrain.

---

* Corresponding author at: Department of Earth Sciences, Vrije Universiteit Amsterdam, 1081 HV Amsterdam, the Netherlands & School of Environmental Studies (ENVI), University of Victoria, V8W 2Y2 Victoria, BC, Canada.

E-mail addresses: nspeetjens@uvic.ca, niek.j.speetjens@gmail.com (N.J. Speetjens).

https://doi.org/10.1016/j.scitotenv.2024.170931
Received 17 July 2023; Received in revised form 29 January 2024; Accepted 10 February 2024

1. Introduction

Global temperatures are rising fast and climate domains are shifting, especially in the Arctic. Here, local temperature increases have exceeded 5 °C in four decades (Rantanen et al., 2022), precipitation regimes are becoming more rain dominated (Bintanja and Andry, 2017), and the pan-Arctic watershed is showing larger and more heterogenous water export (Feng et al., 2021). These changes are largest in the Arctic's northernmost regions, that host innumerable small, low-gradient river catchments underlain by carbon-rich continuous permafrost soils (Speetjens et al., 2023; Vonk et al., 2023) (Fig. 1A,B). Although large uncertainties remain, an estimated 1014 Pg carbon is expected to be stored in the upper 3 m of Northern Hemisphere permafrost regions (Hugelius et al., 2014; Mishra et al., 2021), roughly a third (~330 Pg C) of which is stored in climate-sensitive thermokarst landscapes (Olefeldt et al., 2016) and at least 29 Pg C in the upper 30 cm of soils north of the circumarctic tree line (Bartsch et al., 2016). Thaw and mineralization of this carbon may lead to positive feedback to climate warming (Schuur et al., 2008), yet we still lack a proper understanding of complex and terrain-specific mobilization mechanisms and pathways (e.g., Vonk et al., 2019).

One specific permafrost terrain type susceptible to developing thermokarst is ice-wedge polygon (IWP) terrain (Liljedahl et al., 2016). IWP terrain is common in low-gradient arctic tundra, covering approximately $\sim 3.12 \times 10^6$ km^2 of the northern circumpolar permafrost domain (Karjalainen et al., 2020), and ubiquitous in small northern coastal catchments (Speetjens et al., 2023) (Fig. 1C). IWPs form by frost cracks in the soil, which expand by the repeated freezing of infiltrated water. This displaces soil into elevated rims around lower-lying centers (i.e., low-centered polygons: LCP) (Fig. 2A). As climatological conditions change and ground temperatures increase, ice wedges can melt, resulting in subsidence of rims. Troughs form and drain water from the polygon center. When fully degraded, IWPs have high centers relative to their troughs (i.e., high-centered polygons: HCP). When fully developed, these troughs connect, thereby effectively draining the landscape (Liljedahl et al., 2012; Liljedahl et al., 2016) (Fig. 2B). Hence, ice-wedge degradation and subsequent polygon inversion are likely to drastically change the landscape and its hydrological and biogeochemical functioning locally. Yet very little is known about the quantitative implications of these shifts on a larger scale. Moreover, field measurements are often constrained in time, leading to a 'summer bias' in records of hydrological and biogeochemical variables (e.g., Helbig et al., 2013; Koch et al., 2018; Coch et al., 2020; Speetjens et al., 2022).

Current earth system models (ESMs) lack accurate incorporation of soil organic carbon (SOC) stocks (e.g., Mishra et al., 2017) and controls on hydrology and biogeochemistry in response to changes in IWP terrain (Andresen et al., 2020). On the other hand, current small-scale and terrain-specific models are detailed and focused on specific components of the system (e.g., Wales et al., 2020; Harp et al., 2020; Zlotnik et al., 2020; Jafarov et al., 2022; Mohammed et al., 2022). While these high-resolution models are vital for gaining fundamental insights, translating these into planetary-scale models is difficult (e.g., Nitzbon et al., 2021). Hence, we deem it necessary to develop models that can improve understanding of climate change impacts while taking micro-scale effects into account and simultaneously maintaining scalability to ESM level. Here, we present a new, simple, conceptual model linking hydrology and active layer dynamics in IWP landscapes. The model only simulates intact versus degraded polygons (i.e., LCP vs. HCP) and simulates DOC fluxes from both terrain types on a catchment scale. Our aim is to gain first-order estimations of current discharge for both terrain types, as well as active layer depth and their combined (discharge and active layer depth) relation to DOC flux, as well as insight into the response of these polygon systems to future changes in climate. We also show the utility of a terrain-type-focused conceptual modelling approach to upscale lateral fluxes in permafrost regions and open the door for a discussion about optimizing input parameters from field measurements to help better constrain models linking permafrost terrain to lateral fluxes.

2. Methods

2.1. Model description and definition of components

2.1.1. Model description

We developed a flexible conceptual model for catchments of a specific terrain type: small, low gradient, polygonal tundra, which (to our knowledge) has not been modeled in such a way before. Following principles described by Fenicia et al. (2011), 'conceptual' herein means that we describe the hydrological functioning based on our understanding of the real-world system and on empirical relationships found

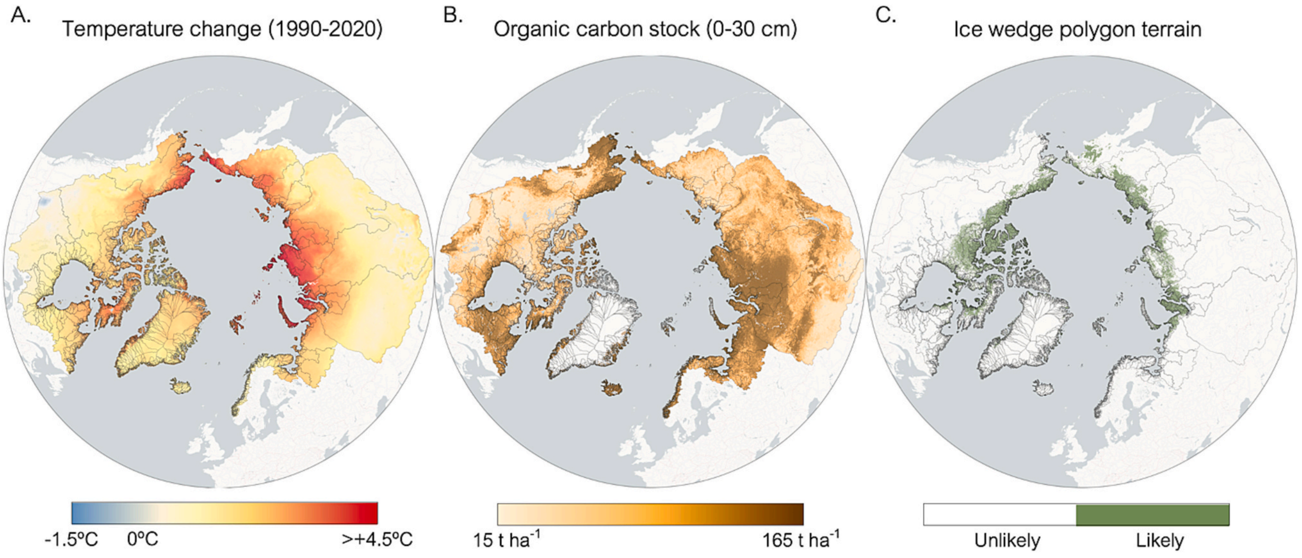

Fig. 1. Major terrain and climate features of pan Arctic watersheds. A. mean temperature increase over the period 1990–2020 calculated using ERA5-Land daily data (Muñoz-Sabater et al., 2021), B. soil organic carbon stocks in the upper 30 cm of the soil as predicted in the SoilGrids database (Poggio et al., 2021) and C. the spatial coverage of ice wedge polygon terrain as predicted by Karjalainen et al. (2020). The background of each image indicates the delineations of catchments draining into the Arctic Ocean as produced by Speetjens et al. (2023).

through field observations. 'Flexible' means that we use a multi-component approach to model catchment-scale processes, and that the components can be substituted, complemented, or adapted into other models.

The model is set up using a binary definition of LCP and HCP (Fig. 2), assuming a respective static geomorphology together with active layer fluctuation as the key determinants of hydrological functioning and DOC flux. In our geomorphological setup we emulate a less well-drained (in the case of LCP) to a more well-drained (in the case of HCP) duality (Liljedahl et al., 2016). We do not simulate all intermediate states of IWP degradation as well as other landscape types and no interaction between the two polygon types. The model assumes LCP and HCP to be on both extreme ends of the permafrost degradation spectrum, which implies that LCP have ice wedges and fully intact rims, whereas HCP have advanced degraded ice wedges and fully developed troughs (Fig. 2.). This implementation of LCP and HCP follows current scientific understanding of ice-wedge polygon evolution (e.g., Kanevskiy et al., 2017).

2.1.1.1. Snow dynamics and insulation. Governing meteorological conditions: daily precipitation *(P)* and temperature *(T)* are the same for both LCP and HCP modules. Snowpack storage (S_{snow}) and snowmelt (Q_{melt}), which are calculated for each time step (d*t*) follow a degree-day model (Hock, 2003) (Eqs. (2.1) and (2.2) respectively):

$$\frac{\mathrm{d}S_{snow}}{\mathrm{d}t} = P_{snow} - Q_{melt} \tag{2.1}$$

where:

$$P_{snow} = P \ if \ T \leq T_{snow} \tag{2.2}$$

and:

$$Q_{melt} = k_{melt}(T - T_{snow}) \ if \ T > 0^{\circ}\mathrm{C}, \mathrm{S}_{snow} > 0 \tag{2.3}$$

with

$$k_{melt} = \overline{k_{melt}} \cdot \Delta k_{melt} \cdot cos\left(\frac{n \cdot 2\pi}{365}\right) \tag{2.4}$$

where n is the day number of the year and $\overline{k_{melt}}$ (mm°C^{-1}d^{-1}) and Δk_m (−) can be chosen to reflect the self-insulating properties of snow, variable over the year. The assumption made here is that as the season progresses the snowpack self-insulates better due to a variety of factors, such as compaction and a lowering of the humidity of the snowpack and the air as the winter cold forces the air to lose its water. Although using a sine function is a simplistic way to implement seasonal variation of the melt constant, e.g., Hock (2003) suggests seasonally variable melt constants as well. Additionally, we implement a snow redistribution factor f_{snow} [0,1] which accounts for snow being trapped in troughs, following observations by Liljedahl et al. (2016), who found significant impact on seasonal runoff distribution caused by snow storage in polygon troughs. The amount of snow that can be trapped is dependent on the depth of the trough (d_{trough}). Once the trough is full, snow continues to accumulate evenly on the surface. The redistribution of snow influences generated surface runoff, as snowmelt from troughs is counted as direct surface runoff. Due to snow redistribution, shallower snowpacks result on the polygon centers, which promote winter soil freezing.

Finally, we use so called effective precipitation as the influx of water in each timestep, calculated as:

$$P_z = P + Q_{melt} \tag{2.5}$$

Snowpack depth insulates the soil and thereby impacts the freezing and thawing of the seasonal active layer. Hence, we estimate the snowpack depth (mm) by rewriting the empirical relation stated in Eq. (1) by Hill et al. (2019):

$$z_{snow} = 5.73192 \cdot \mathrm{S}_{\mathrm{snow}}^{0.907441} \tag{2.6}$$

which is then used to calculate freezing and thawing n-factors for following Gisnås et al. (2016, 2017):

$$n_f = -0.16 ln z_{snow} + 0.22 \tag{2.7}$$

and:

$$n_t = -0.14 \ z_{snow} + 1.1 \tag{2.8}$$

Evapotranspiration is calculated using Hamon's (1961) equation

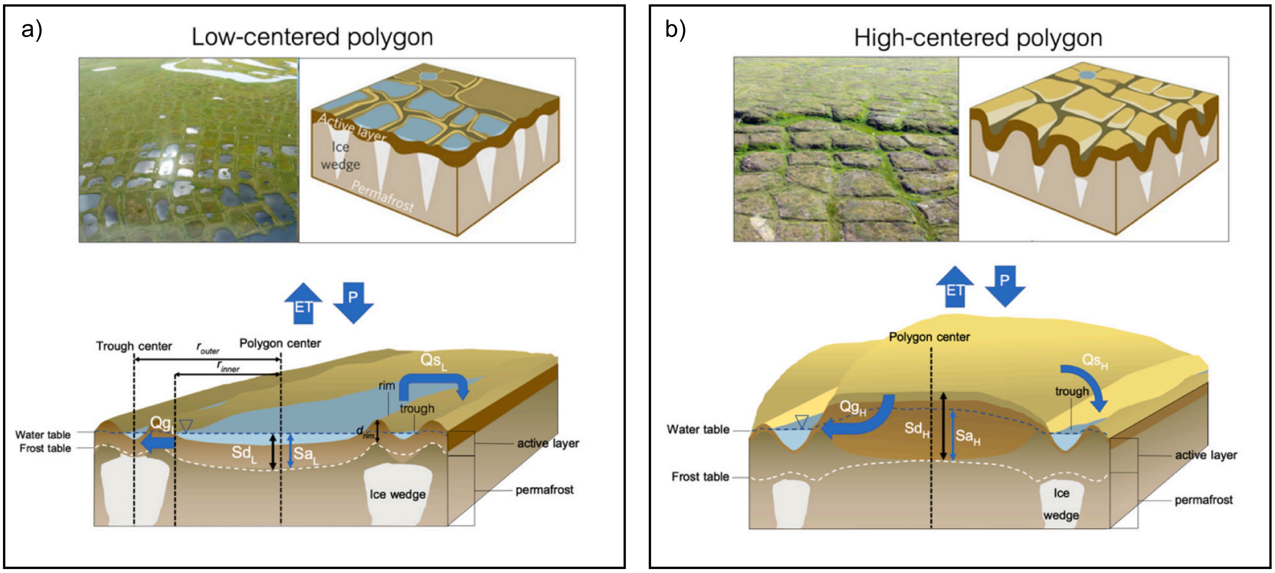

Fig. 2. Conceptual overview of the hydrological functioning of low-centered (a) and high-centered (b) polygons in the model. Runoff generated through groundwater flow in low-centered polygons (Qg_L) is limited by the thickness of the active layer at the rim (d_{rim}) the thickness of the rim ($b_{rim} = r_{outer}$ - r_{inner}) and the hydraulic gradient between the storage in the active layer ($h \sim Sa_L \sim$ saturated thickness) and the trough ($h \sim 0.1d_{rim}$). Our model scales d_{rim} with the depth of the active layer such that flow always occurs toward the trough). Low-centered polygon functions through a fill and spill mechanism in a way that surface runoff (Qs_L) is generated when $Sa_L \geq Sd_L$. Note that Sd_L does not have to be equal to Sa_L. High-centered polygons are modeled as a linear reservoir; drainage occurs through groundwater flow (Qg_L) which is a function of available storage (Sa_L) divided by a time constant. When $Sa_H \geq Sd_H$ surface runoff (Qs_H) is generated (top row figures of ice-wedge polygon terrain were adapted from Liljedahl et al., 2016).

using the PyET python module (Vremec and Collenteur, 2021, an open-source project on Github (www.github.com/pyet-org/PyEt), using the daily average temperature and latitude to determine daylight length for each time step. Here, we use potential evapotranspiration as actual evaporation under the assumption that water is not a limiting factor in the polygonal tundra landscape and that evaporation is relatively constrained due to low air temperatures and low solar irradiation.

2.1.1.2. Active layer evolution. Seasonal active layer evolution is a major controlling factor for hydrology in permafrost-affected regions. Hence, for every timestep we calculate the change in the active layer depth using the Stefan equation for soil thawing as presented by Kurylyk and Hayashi (2016):

$$X(t) = \sqrt{\frac{2k_u I(t)}{\phi \rho_w L}} \tag{2.9}$$

k_u is the bulk thermal conductivity of the frozen/unfrozen zone ($\mathrm{W\,m^{-1}\,K^{-1}}$) where $k_u = \left(\theta_w k_w^{0.5} + \theta_m k_m^{0.5} + \theta_o k_o^{0.5} + \theta_a k_a^{0.5}\right)^2$ and $\theta_{w,m,o,a}$ are the volumetric fractions of water, mineral solids, organic solids and air in the soil and $k_w = 0.57$, $k_m = 3.8$, $k_o = 0.25$, and $k_a = 0.025$ their respective thermal conductivities ($\mathrm{W\,m^{-1}\,K^{-1}}$) for thawing, for freezing the conductivity of water is substituted by that of ice, $k_i = 2.2$ (Hillel, 2013). X is the depth (m) of the thawing front, ϕ is the volumetric moisture content of the thawed zone, ρ_w is the density of water ($\mathrm{kg\,m^{-3}}$), L is the mass-based latent heat of fusion for water ($3.34 \times 10^5\,\mathrm{J\,kg^{-1}}$), t is time and I is the surface freezing index calculated by integrating:

$$I(t) = \int_0^t T_s(t)\mathrm{d}t \tag{2.10}$$

where T_s denotes the daily surface temperature. I can then be multiplied by daily nF or nT to correct for surface properties affecting freezing or thawing, such as the presence of a snowpack. Finally, we calculate the daily active layer depth (m) as the sum of the freezing and thawing depths:

$$ALD(t) = \sum_{t=0}^{t} X_{thaw}(t) - \sum_{t=0}^{t} X_{freeze}(t) \tag{2.11}$$

Soil parameters $\theta_{m,o}$ for LCP and HCP can be defined separately, and because of the inherent drainage differences the seasonal active layer will develop differently between LCP and HCP, resulting in different soil storage and runoff.

2.1.1.3. Storage and runoff. The model assumes the potential storage depth for water in the soil to be the entire pore volume of the active layer at each timestep, defined as:

$$S_d(t) = ALD(t)\cdot\varphi \tag{2.12}$$

where ALD is the active layer depth for LCP or HCP at each timestep and φ is the porosity of the soil in LCP or HCP. The actual storage in the active layer is defined following a simple water balance:

$$\frac{\mathrm{d}S_a}{\mathrm{d}t} = \frac{\mathrm{d}S_d}{\mathrm{d}t} + P_z - ET - Q_g \tag{2.13}$$

At the current state, the model assumes that infiltration rates (i.e., flow of P_z into S_a) are not hampered by soil surface properties, as these are generally consisting of porous organic-rich materials in the environment described by the model. Hence excess runoff is only generated when the active storage capacity S_a is exceeded.

For the low-centered polygon, we calculate drainage according to the model proposed by Zlotnik et al. (2020). Given the extensive mathematical explanation, we refer to their publication for details. In our simulations a fixed head h_{trough} in the trough was chosen, however this can be varied according to the user's preference. Initial head (H_0) in the polygon center was set equal to the rim height (b_{rim}). K_{sat} is the horizontal (radial) saturated conductivity of the LCP soil ($\mathrm{m\ d^{-1}}$). We assumed a constant anisotropy ratio of 10, where $K_{vertical} = \frac{1}{10}K_{sat}$. We assume the interface thickness $l = c\,ALD$ (with c [0,1]) which represents a slightly shallower active layer in the polygon rim than in the center thereby constraining the flow through interface (l).

For high-centered polygons, we assume drainage following the linear reservoir concept:

$$Q_{g_H} = \frac{S_{aH}}{\tau} \tag{2.14}$$

where τ is a drainage timescale (d) for an HCP linear reservoir which we estimated to range between 1 and 100 days.

Other model assumptions include that for both polygon types, the surface runoff Q_s is generated if $S_a > S_d$. The model applies to continuous permafrost (i.e. an impermeable layer underneath the active layer) areas only and the active layer consists of 1 homogenous layer. Hydraulic conductivity for flow through the LCP rim is isotropic.

2.1.1.4. Water residence time and DOC module. We calculate [DOC] using a production-decay model as presented in Jepsen et al. (2019):

$$[DOC](t-t_0) = \frac{a10^{0.04T_s}}{kT_s} + \left([DOC](t_0) - \frac{a10^{0.04T_s}}{kT_s}\right)e^{-kT_s\tau(\mathrm{t}-\mathrm{t}_0)} \tag{2.15}$$

Here a ($\mathrm{mg\ L^{-1}d^{-1}}$) is a production coefficient, and k ($\mathrm{{}^\circ C^{-1}d^{-1}}$) a first-order rate constant that can be calibrated such that [DOC] reflects values observed in the study area. Jepsen et al. (2019) used values of 0.11 mg $\mathrm{l^{-1}}$ $\mathrm{day^{-1}}$ and 7.5×10^{-3} $\mathrm{{}^\circ C^{-1}}$ $\mathrm{day^{-1}}$, respectively for a and k. The residence time, or 'age' of water in the soil, τ (d), is calculated via a mass balance. In addition, we account for the freezing and melting of water in the soil as the seasonal active layer evolves, which leads to the addition or removal of water of a certain age from the active storage as the soil thaws or freezes. This leads to the following equations:

$$\tau(\mathrm{t}-\mathrm{t}_0) = \frac{2V_{mean} + 2\tau(\mathrm{t}_0)\mathrm{q}_{\mathrm{in}} - \tau(\mathrm{t}_0)q_{out} + 2V(t_0)\tau(\mathrm{t}_0)}{q_{out} + 2V(t-t_0)} \tag{2.16}$$

where $V_{mean} = 0.5(V(\mathrm{t}_0) + V(\mathrm{t}\text{-}\mathrm{t}_0))$ is the mean volume of water in storage ($V = S_a$). Then, as the active layer refreezes, the age of water is "locked" for the time when frozen. When the active layer thaws again this water is added to the storage volume and the age of the total active layer is calculated as the weighted mean of the ages of active storage and the additional meltwater.

2.2. Model parameterization and simulations

2.2.1. Baseline study area data

Catchment studies that quantify fractions of LCP and HCP, discharge, and [DOC] are sparse. For example, a field study by Jones et al. (2023) quantifies fractions of LCP and HCP in an area on Svalbard to study differences in their biogeochemical properties but does not quantify runoff. On the other hand, Helbig et al. (2013) study hydrology in polygons at various degradation stages (i.e., along the LCP-HCP transition axis) but lack biogeochemical measurements. Similarly, model studies such as Zlotnik et al. (2020) quantify both water and DOC flux but focus only on LCP, while Liljedahl et al. (2012) showcase a model to illustrate how catchment drainage is controlled by polygon type but leave out the coupling with biogeochemistry. Here we test and calibrate our model using field measurements of discharge and [DOC] at the catchment outlet of Ptarmigan Bay, a study site along the Yukon Coast, Canada (69.465°, −139.125°). Using satellite imagery Worldview-3 imagery (DigitalGlobe 18 July 2018) and object-based classification method (Blaschke, 2010), we classified catchment LCP and HCP fractions. The catchment area is ~4 $\mathrm{km^2}$ of which approximately ~96 % is classified as IWP terrain (4 % consisted of larger open water bodies such as lakes and larger ponds which we do not include in our model). Of the IWP terrain ∼28 % is classified as LCP and 72 % is classified as HCP (Fig. S2). DOC samples ($[\mathrm{DOC}]_{\mathrm{mean}} = 16.89 \pm 0.7$ mg L^{-1}) and discharge ($Q_{\mathrm{mean}} = 1.45 \pm 1.1$ mm d^{-1}) measurements were collected during a single sampling period of 10 consecutive days in August 2018 (Speetjens et al., 2022). Additionally, soil property data is used from a total of 40 soil cores spread out evenly across the catchment. We use soil parameters shown in Table 1. In field settings, soil properties are known to vary between troughs, rims, and polygon centers (e.g., Wales et al., 2020), however in our model we use bulk porosity to calculate soil water storage capacity and active layer development in the polygon center. Hence, we averaged only polygon center soil properties from the field measurements. Other hydraulic parameters, such as hydraulic conductivity and drainage timescale τ, are estimated.

We use temperature and precipitation data from ERA5-Land Daily Aggregated data because of its global coverage and uninterrupted temporal coverage from 1963 to the present (Muñoz-Sabater et al., 2021). The spatial resolution is 0.1° x 0.1° (∼9 km × 9 km at the field site), which we deem sufficient for our study. Table S1 summarizes all parameters for the base model run. We run the model using the ERA5-Land data for temperature and precipitation over the period 01-01-2000 to 31-12-2020, using the first year as a spin-up period (Fig. S1).

2.2.2. Climate scenario simulations

We run the model using future climate scenarios from an arctic-focused climate model: CORDEX – ARC-CanESM2 (Copernicus Climate Change Service, Climate Data Store, 2019, accessed: 14-03-2023). This data follows the same global forcing scenarios as CMIP6 (e.g., RCP45, RCP85, etc.) but is specialized to simulate future climates for specific regions.

To simulate the possible future response of IWP catchments to climate change, we ran various climate forcing scenarios using the RCP45 (i.e., stabilization of radiative forcing at 4.5 W m^{-2} by 2100 (Moss et al., 2010)) data series: Firstly, we evaluated a baseline period (01-01-2011 to 31-12-2020), a mid-century period (01-01-2051 to 31-12-2060) and a late-century period (01-01-2091 to 31-12-2100). Locally, Arctic temperature trends have exceeded 1.25 °C decade^{-1} over the past 42 years (Rantanen et al., 2022). To test the effect of similar temperature increases in the future, we ran our model by increasing the baseline period temperature by 1 °C to 9 °C (with 1 °C increments). Similarly, we tested the effect of increasing and decreasing summer precipitation (e.g., McCrystall et al., 2021) by assuming summer precipitation increases up to 150 % and reductions down to 50 % of current day precipitation as well as an increased temperature of 4.5 °C (compared to the baseline period). We ran all scenarios over a range of fractional coverage of HCP versus LCP to get an understanding of how this ratio influences catchment runoff and DOC flux. The model parameter setup was the same for all runs (Table S2).

2.3. Catchment-scaled field data

To compare our model results with field data on a catchment scale, we mapped polygon type, active layer depth, and soil DOC concentrations (Fig. S2) based on field measurements and high-resolution satellite data. These maps were then used to calculate average soil DOC concentrations and estimates of soil DOC stocks (at the time of sampling) for each polygon type in the catchment. We then compared the stocks to the modeled and calculated field-based fluxes to get an idea of the relative magnitude of stock versus flux and the relative contributions of each polygon type to lateral flux out of the catchment.

Table 1

The mean ± SD of porosity and volumetric fractions of mineral and organic solids and water in the active layer (∼0–50 cm) of LCP and HCP landforms in samples taken from Ptarmigan Bay catchment. (Volumetric fraction of air is calculated as 1-($\theta_m + \theta_o + \theta_w$)).

	Porosity (φ)	Mineral (θ_m)	Organic (θo)	Water (θ_w)
LCP	0.37 ± 0.1	0.25 ± 0.2	0.38 ± 0.2	0.19 ± 0.1
HCP	0.34 ± 0.1	0.28 ± 0.2	0.37 ± 0.2	0.19 ± 0.1

2.3.1. Mapping of soil DOC and active layer depth

Maps of soil DOC and active layer depth for the catchment area were produced following the workflow of Wagner et al. (2023). Point data for active layer depth, DOC in the lower active layer and upper permafrost were trained and predicted with random forest (Breiman, 2001) on the same input variables as used in Wagner et al. (2023). Training data for DOC were based on measured DOC from extracted porewater from Speetjens et al. (2022). Active layer depth data are from Wagner et al. (2023) and were taken during the same sampling campaign by using a soil probe at the sampling site.

2.3.2. Classification of polygon type

The landform classification is based on object-based image analysis (OBIA) (Blaschke, 2010). This is a concept applied to high-resolution satellite imagery where features that are composed of several pixels are integrated into objects. In our study, we use a combination of segmentation in eCognition and classification in R using the random forest algorithm on a Worldview-3 image (DigitalGlobe 18 July 2018). The panchromatic band of the Worldview-3 (WV-3) image was used to compute the following filters: Edge extraction canny in eCognition, black-hat, and top-hat filter in SAGA GIS with the tool Morphological Filter (OpenCV) (Conrad et al., 2015). The latter was calculated using the element shape “ellipse” and a radius of 5 cells. Witharana et al. (2021) used black-hat and top-hat filter operations as input to distinguish trough features in polygonal tundra, which shows that these filters can be used successfully in OBIA applications. The first step of the segmentation process was excluding rivers and water bodies from the land area using the multi-threshold resolution based on NDVI <0.25. Subsequently, the multi-resolution segmentation method was used, including the canny edge extraction filter, black-hat, and top-hat with layer weights of 5, 1 and 1, respectively. The scale parameter was set to 10, Shape and Compactness were to 0.1. The resulting segments were exported including 81 segment properties based on geometry and average values of WW3–3 bands and vegetation indices. Prior to the application of the random forest algorithm in R (R Core Team, 2021), a pre-selection of the most important variables was computed using the package Boruta (Kursa and Rudnicki, 2010). The Boruta package is a wrapper around the package *randomForest* (Liaw and Wiener, 2002). It creates duplicates, called shadow features, from each variable and runs a random forest algorithm. Variables that score significantly higher than their respective shadow features are selected as important and variables scoring significantly lower are defined as unimportant. Ground truth points were collected in the field during the field campaign in the summer of 2018. Additional training points were selected based on visual interpretation of the WV-3 image. Segments underlying these training points were used as respective training segments. A random forest was then trained on 31 parameters (Table S3) and the segments were classified into HCP, LCP and no Polygon, the latter representing water bodies. The model was validated using 3-fold cross-validation. The accuracy of the model was 0.90 and Kappa was 0.83.

2.3.3. Calculation of DOC stock and flux

From the soil DOC concentration, polygon type, and active layer depth maps, we calculated the soil DOC stock (gC m^{-2}) in each pixel as:

$$DOC_{stock} = \frac{[DOC] \times \overline{\theta_w} \times ALD}{1000} \tag{2.17}$$

where $[DOC]$ is the DOC concentration (mg L^{-1}), $\overline{\theta_w}$ is the mean annual soil water fraction (−) taken from the model output, and ALD is the active layer depth (mm). Because of its complexity soil DOC stock is not very often calculated in studies concerning carbon budgets, yet we deem it useful as it is more directly linked to DOC flux than SOC stock (i.e., the solid fraction or total of OC in soils).

3. Results and discussion

3.1. Model test case Ptarmigan Bay

3.1.1. Runoff

For the base run we simulated the Ptarmigan Bay catchment over the period 2001–2020 (20 years). Our model produces distinct patterns in runoff for LCP and HCP (Fig. 3A). Both LCP and HCP show peaks in discharge: LCP-runoff most notably peaks during spring freshet (as surface and shallow subsurface runoff), which indicates that this runoff is mostly caused by snowmelt. LCP also has a flattened peak of groundwater flow toward the end of the summer season as the active layer reaches its annual maximum. HCP-runoff peaks as surficial runoff from trough-trapped snow during freshet and in a broader peak of subsurface runoff over the late summer season. HCP-surface runoff during summer is negligible (depending on model setup and meteorological input data). Surface runoff is only generated during snowmelt in both HCP and LCP, and when the active layer is still relatively shallow (Fig. 4C) and the storage is most saturated (Fig. 4A,B). As active layers develop throughout the season, HCP storage is generally not fully saturated hence only sub-surface runoff is generated (Fig. 4B).

Available runoff data (August 2018) (Speetjens et al., 2022) align with how the model was set up (i.e., a combined fill and spill and linear reservoir mechanism for LCP and a linear reservoir mechanism for HCP). We additionally ran the model for a field site on Samoylov Island, Russia, for which a longer series of runoff data were available (June 2014 – September 2014) (Beckebanze et al., 2022). Here, the model produced agreeable results too (Fig. S2). For the main focal site (Ptarmigan Bay catchment), the total runoff ($Q_{catchment} = 1.47 \pm 0.2$ mm d^{-1}) is the sum of LCP, HCP, and excess runoff (i.e., overland flow) and corresponds with the mean observed runoff ($Q_{obs} = 1.45 \pm 1.1$ mm d^{-1}). However, the relative standard deviation of the measured discharge was high due to a constructed rating curve, based on flow measurements taken by hand using a flow meter and by measuring the cross-sectional area of the stream (Speetjens et al., 2022). The modeled discharge, on the other hand, only uses daily precipitation data and calculates runoff on a daily timestep. Moreover, the precipitation data stems from a 0.1° x 0.1° resolution dataset. This means that local precipitation peaks are likely not well represented in the precipitation data and that short peak discharge events such as measured in the field, which often occur during shorter periods in these small catchments than the 1-day timestep used

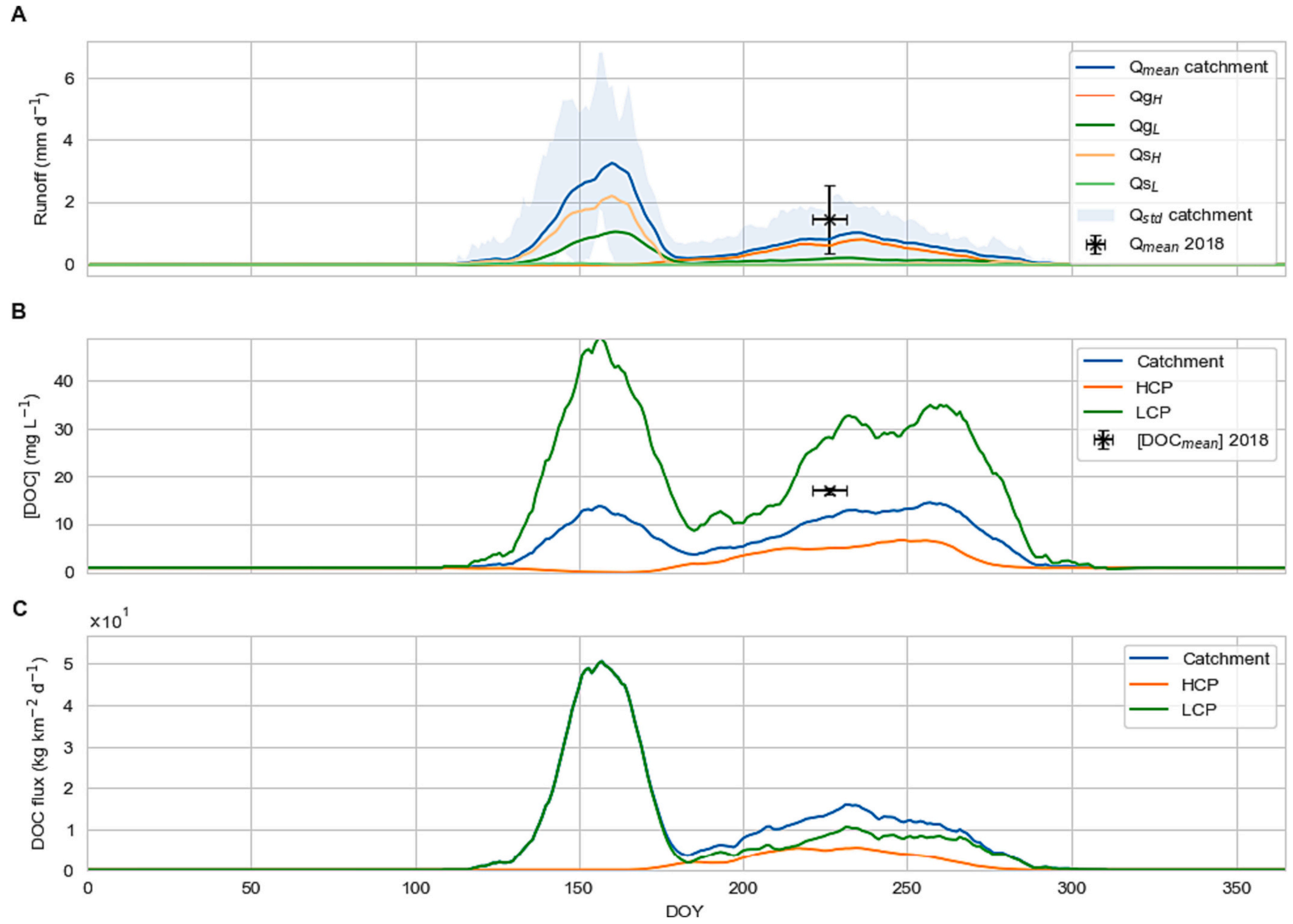

Fig. 3. Modeled seasonal long-term (20 year) average discharge, [DOC] and DOC flux for field site Ptarmigan Bay using ERA5-Land temperature and precipitation data over the period 2001–2020. Panel A shows the runoff (mm d^{-1}) generated for both landforms as the long-term daily average of groundwater flow: Qg_H (orange), Qg_L(green), catchment total (blue) and surface runoff: Qs_H (red) and Qs_L (purple). Panel B shows the DOC concentration (mg L^{-1}) of runoff of both landforms and the weighed outlet runoff DOC concentration (blue). Panel C shows the calculated total DOC flux (kg km^{-2}d^{-1}) of each landform and the catchment total. The fraction catchment coverage of HCP = 0.72, (LCP = 0.28). Black markers show the average discharge and DOC concentration as measured in the field in 2018 over a period of 10 days.

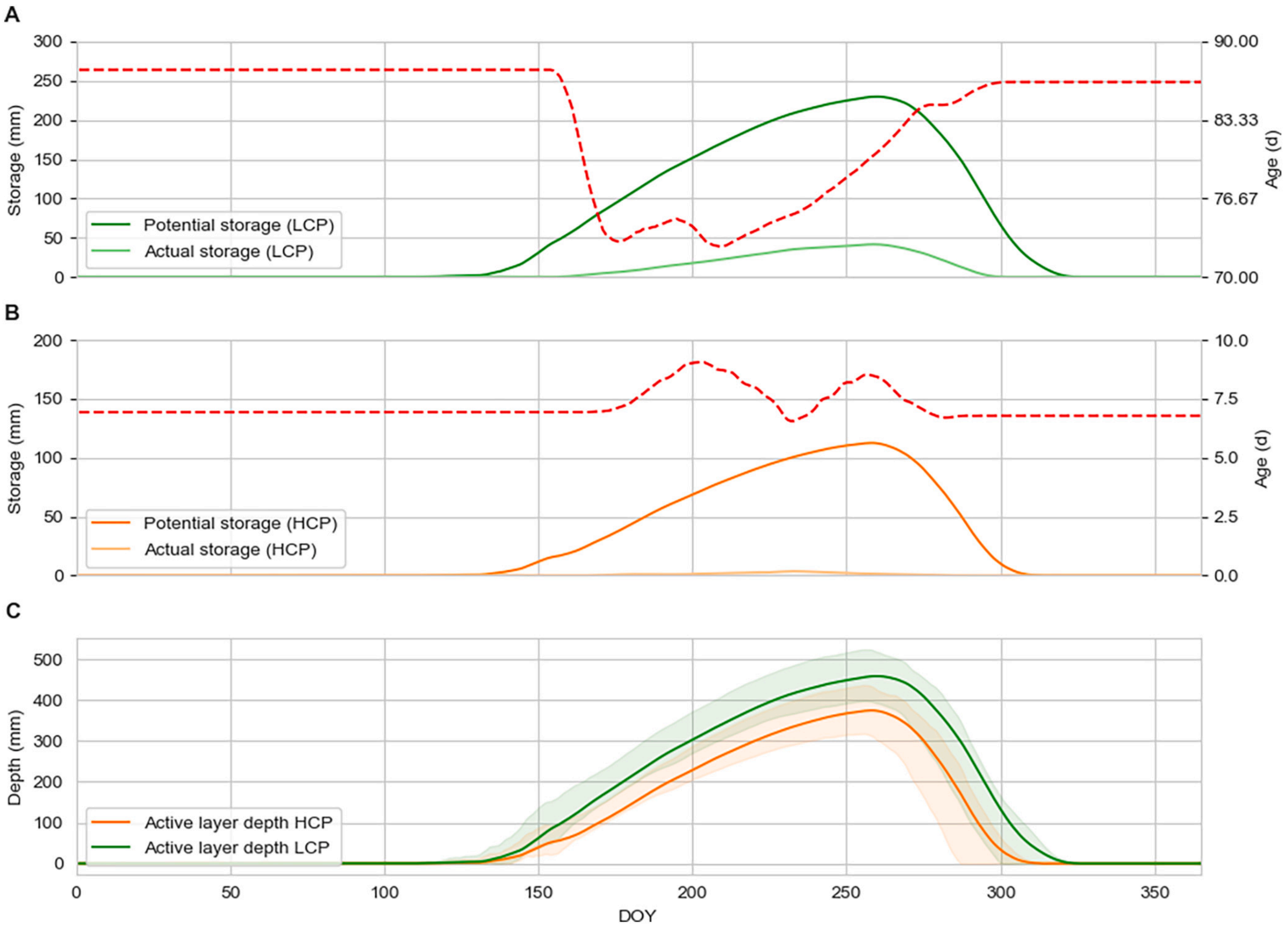

Fig. 4. Modeled seasonal long-term average soil storage for LCP (A), HCP (B) and active layer dept. evolution for both polygon types (C), using ERA5-Land temperature and precipitation data over the period 2001–2020. Graphs show the daily mean over this period. Red dashed lines show the mean water age of the outflowing water. The fraction catchment coverage of HCP = 0.72, (LCP = 0.28).

in our model, are omitted.

Our model indicates that, aside from freshet peaks in both LCP and HCP (troughs), the majority of summer runoff is coming from LCP while HCP sub-surface runoff only starts playing a significant role toward the end of the season. We suggest this is caused by differences in the groundwater storage capacity which is more likely to be saturated in LCP than in HCP due to LCP's microtopographic layout (i.e., elevated rims) compared to that of HCP (troughs). This is in line with field observations of Helbig et al. (2013) which show that microtopographic variations dictate runoff behavior. However, their study suggests that late summer runoff is mostly generated by intact polygons (i.e., LCP), while degraded polygons (i.e., HCP) generate runoff only during snowmelt. They conclude that the barrier function of LCP rims is controlled by soil thaw (which is also the case in our model) and that therefore soil thaw dynamics control the timing and magnitude of subsurface runoff. The differences in timing and magnitude in our model are a result of the model parameterization. Soil water storage is not saturated during the deepening of the active layer in HCP at the start of the season, which leads to the runoff of remaining snowmelt at the polygon center through the soil rather than over the surface in our model (while in reality surface runoff may still dominate because of saturated conditions). Since we did not include a maximum infiltration rate, infiltration is possibly overestimated. However, given the organic rich nature of the soil and surface in these polygon-tundra landscapes we deem the unconstrained infiltration during active layer thawing realistic. With more site-specific field data it is possible to adjust the thawing ratio of the rims as well as the hydraulic conductivity (e.g., to increase runoff that is generated from LCP), thereby making the model match field observations better.

3.1.2. *Active layer development*

Seasonal active layer development is mainly controlled by air temperature and soil bulk thermal conductivity (Kurylyk and Hayashi, 2016). Our model produces seasonal patterns in active layer depth, with thaw initiation at day ~140 and fully refrozen conditions by day ~350. Our model results reflect active layer depths measured in the field during the 2018 sampling campaign. Several studies have described seasonal active layer depths, which range between ~0.3 and ~ 1.5 m along the Yukon coast (Burn, 1997; Kokelj et al., 2002; Fritz et al., 2012), but 2018 was a relatively cold year. Our model consistently produces shallower maximum active layer depths in HCP (107.8 ± 12 cm) than in LCP (145.5 ± 16 cm) (Fig. 4C), which reflects what was observed in the field (Fig. S2). We modulate the active layer depths based on calibration with field measurements, thereby accounting for insulative surface properties. As such, we do not include a module that simulates insulative vegetation layer dynamics throughout the season. Nitzbon et al. (2019) report the effect of organic layers on bulk thermal conductivity, which, when drier, insulate the subsurface even better. Incorporating a module that simulates the presence of insulative layers (e.g., mosses) in HCP centers (dryer) and the (relative) absence in LCP centers (wetter/inundated) and their insulative response to dry and wet meteorological conditions is likely to improve the model further. For the purpose of this study we deem our simplification sufficient. Modeled refreezing of LCP in the Fall consistently occurs slower than HCP. The difference in freezing behavior is likely attributable to deeper active layers and higher soil moisture content in LCP, which results in a different thermal conductivity of LCP and higher required latent heat of fusion for the phase transition of water (de Bruin et al., 2021).

3.1.3. DOC concentration and flux at Ptarmigan Bay

Our model shows deeper active layers in LCP than in HCP (Fig. 4C). Due to the microtopographic layout and consequential drainage properties, a larger groundwater storage deficit occurs in HCP compared to LCP. This results in lower average water age in HCP than in LCP (i.e., the total volume of water in storage is smaller hence residence time is shorter), which is also reflected in lower overall DOC concentration in HCP than in LCP (Fig. 4A,B). Modeled mean DOC concentration of the catchment outflux is of the same range (16.01 ± 1.5 mg L^{-1}) as measured mean DOC concentration over the sampling period (16.89 ± 0.7 mg L^{-1}). The model produces DOC concentrations that are higher for LCP (39.59 ± 12.5 mg L^{-1}) than HCP (6.32 ± 1.8 mg L^{-1}), which, based on the model setup, is primarily a result of longer residence time in LCP. The difference in DOC concentration in runoff from LCP and HCP seems to contradict some findings by Coch et al. (2020) who conclude that degrading ice wedge polygon terrain (i.e., transformation from LCP to HCP) could increase DOC concentrations. Also, field data from Speetjens et al. (2022) shows slightly higher DOC concentration in porewaters extracted from HCP compared to LCP, but the difference was not statistically significant, and it is difficult to compare soil pore water and surface water due to large heterogeneities within the soil and uncertainties concerning actual flow paths (e.g., Wales et al., 2020). The model currently does not account for unsaturated zone storage which could increase water residence times and DOC concentrations in HCP (which potentially has relatively large unsaturated storage). Our model assumes the same DOC production coefficients in HCP an LCP and saturated storage only. To better understand the relation of these model parameters to field settings more data and experiments are needed.

Our model shows that the majority of mean annual DOC (0.63 ± 0.6 × 10^3 kg C km^{-2} y^{-1}) is exported by LCP (0.86 ± 0.4 × 10^3 kg C km^{-2} y^{-1}) with HCP (0.09 ± 0.2 × 10^3 kg C km^{-2} y^{-1}) accounting for only about ~10 % of that. In comparison, Speetjens et al. (2022) estimated catchment DOC flux at 2.14 × 10^3 kg C km^{-2} y^{-1}, which, when scaled proportionally to polygon type fraction coverage yields 0.60 × 10^3 kg C km^{-2} y^{-1} for LCP and 1.54 × 10^3 kg C km^{-2} y^{-1} for HCP. A study by Jafarov et al. (2022) used numerical modelling to show that in the presence of only hydraulic gradients as drivers for transport (i.e., the absence of thermal gradients), tracer mobility was limited in LCP while transport of tracers was hydraulic gradient-driven in HCP. This affirms our simulations that residence time in LCP is longer than in HCP. The result in our model is that DOC concentration is higher in LCP and in terms of net-seasonal flux it appears that LCP is responsible for the largest fraction of DOC output. To our knowledge, there is currently no research that quantifies DOC flux in ice wedge polygon terrain, differentiated by polygon type. Beckebanze et al. (2022) suggest that lateral carbon flux (i.e., DOC and DIC (dissolved inorganic carbon) flux in this study) plays only a minimal role with only 2 % of net ecosystem exchange (F_{DOC} = ~60–80 kg C km^2 $season^{-1}$) in the carbon budget of IWP terrain. Although their study site description (for Samoylov Island, Russia) mentions that the catchment features both intact (LCP) and degraded (HCP) polygons, they do not provide polygon-type specific lateral fluxes. From visual inspection of the satellite imagery included in their work, their study area seems predominantly covered by LCP. The total seasonal runoff in the catchment studied by Beckebanze et al. (2022) was much smaller: Translated to the same units, the study of found a DOC flux of ~0.7 mg m^{-2} d^{-1} ($[DOC]_{mean}$ = 5.31 mg L^{-1}) between 10 and 19 August 2014. The associated runoff was ~0.2 mm d^{-1}. The study used here (Black Creek; Speetjens et al., 2022) measured a runoff of ~1.45 mm d^{-1} and a related DOC flux of ~22.8 mg m^2 d^{-1} ($[DOC]_{mean}$ = 15.73 mg L^{-1}) during the period 10–19 August 2018. These campaigns were held at different locations and in different years, and while there is some uncertainty regarding the exact catchment area in both studies, there is a significant difference in DOC flux of the two catchments. It is worth noting that this difference in DOC flux seems to stem from both the difference in DOC concentration (~3 times higher in Black Creek) and the difference in runoff (~7 times higher in Black Creek), as this was approximately 3 times higher in the latter study. Considering the uncertainties that come with field measurements, these findings suggest that there is at least significant variability among catchments that at first glance appear similar (i.e., IWP catchments) but are very different (i.e., LCP vs HCP dominated) upon closer examination. This underpins the need for further field studies directed toward comprehending the mechanisms underlying these systems. An important step herein is the qualification and source apportionment of catchment outflux dissolved organic matter (DOM). For example, Speetjens et al. (2022) found significant terrestrial contribution to outflowing DOM, suggesting deeper flow paths associated with HCP. Beckebanze et al. (2022) did not qualify stream DOM but having this information would greatly help explain the differences between the two catchments. IWP terrain covers vast areas of the pan-Arctic watershed (Karjalainen et al., 2020). Hence, more study of differential flow path behavior in IWP terrain (e.g., Wales et al., 2020) and dedicated efforts to improve modelling implementation of IWP catchments are needed, such that these are correctly translated into ESMs.

From our catchment-scale classification and [DOC] maps (Fig. S2) we calculated the average catchment soil porewater DOC stock (in the active layer). For LCP, this is ~12.3 g C m^{-2} or 13.8 × 10^6 g C in total for Black Creek catchment (~4 km^2, ~28 % catchment coverage) and ~ 10.2 g C m^{-2} or 29.4 × 10^6 g C in total for HCP (ca. 72 % catchment coverage). These numbers suggest that about ~7 % of mobilized (i.e., dissolved) organic carbon is exported from LCP systems while ~1 % of DOC in soils is exported from HCP. We acknowledge that these estimates are made based on several assumptions, and more field data and model calibration may be needed to refine insights. Our comparison suggests that although HCP systems are more efficiently drained, resulting in a shorter residence time of DOC (HCP ~7 days; LCP ~96 days, Fig. 4A,B), they account for a relatively small fraction of DOC export under current climate conditions. This may however change under future climate scenarios with deeper active layers, and a more rain-dominated flow regime. This is likely to increase the soil water storage volume in HCP thereby increasing the leaching of SOC in these systems.

3.2. LCP vs. HCP: Seasonal dynamics and future climate

To get an understanding of seasonal runoff and DOC dynamics for LCP and HCP, we ran our model multiple times with a current (2011–2020), intermediate-term (2051–2060) and long-term (2091–2100) climate scenario while gradually increasing the fraction HCP coverage (Fig. 5). For current conditions, a distinction between LCP and HCP exists for the timing of their runoff peaks: LCP has higher and likely shallower runoff during early season while HCP has higher runoff during late season (Fig. 5A). This difference seems to persist in the future climate scenario, and the intensity of the early season peak seems to increase (i.e., higher and shorter) in the future for LCP while for HCP the snow driven early season peak discharge diminishes (Fig. 5B). Additionally, when comparing annual total runoff in 100 % LCP (2011–2020) and 100 % HCP (2091–2100) (i.e., mimicking a transition from LCP to HCP over eight decades), the model runs show a ~ 17 % runoff decrease while this is less (~8 %) when 100 % LCP is maintained. The model runs uniformly show that in a future warmer and wetter climate, the length of the flow season increases (Fig. 5A,B), ~5 % by the end of the century in our runs. The increase of flow length in the real world will vary greatly depending on climate and terrain properties. Although average DOC concentrations do not change much (Fig. 5C,D), the lengthening of the flow season results in a higher annual DOC flux (Fig. 5E,F) toward the

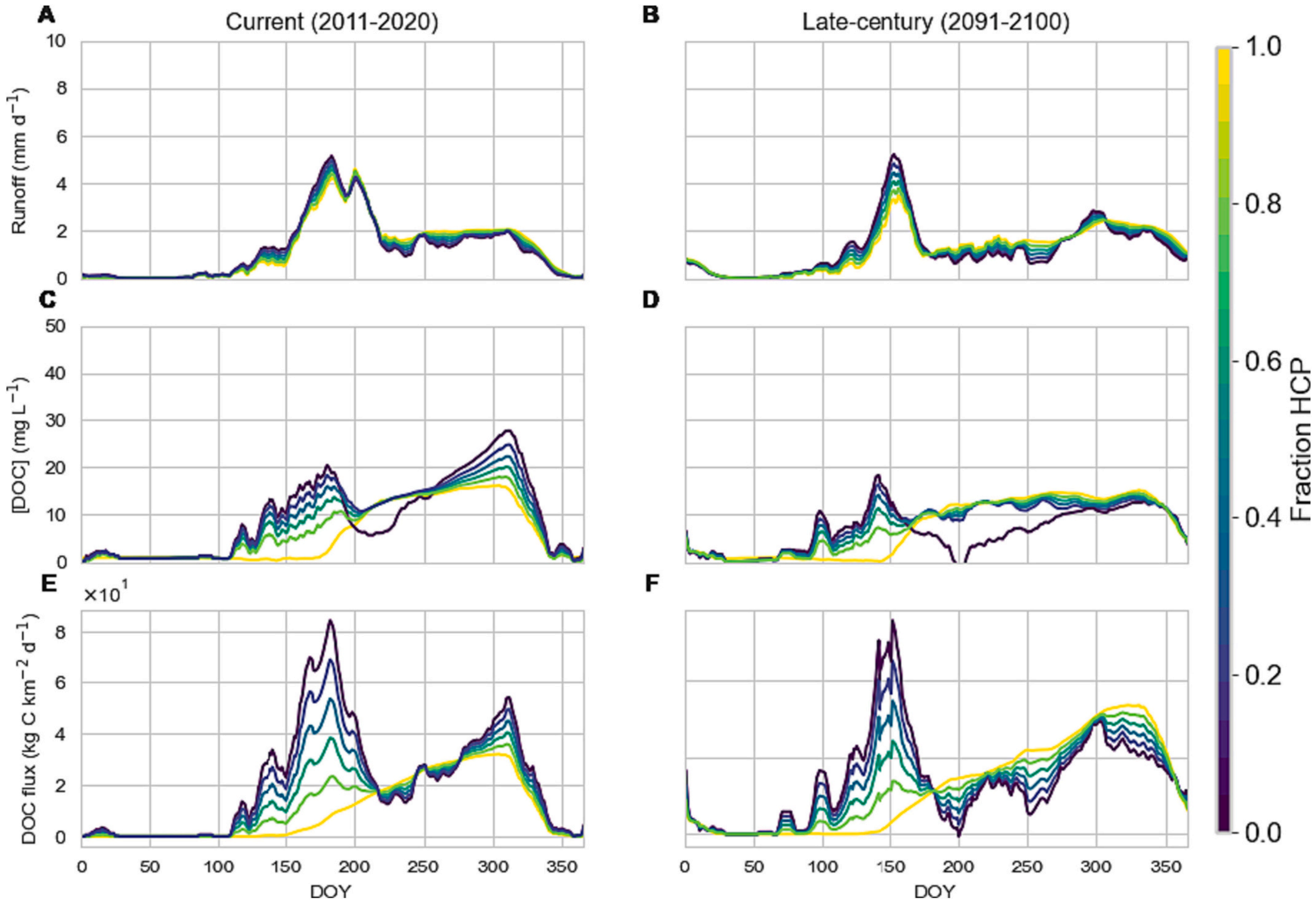

Fig. 5. Current (2011–2020) and late-century (2091–2100) model runs for fraction HCP 0–1. The most important shifts are the lengthening of the flow season in the future climate and the increase in the intensity (shorter and higher) of the freshet flow peak. The result of the former is that annual DOC export from the catchment (area under the third graphs left and right) becomes larger. Aside from some intra-seasonal fluctuations, DOC concentrations are higher in LCP, especially toward the late season. Regardless of this the total DOC flux (area under the graph, lower left and right) decreases as fraction HCP increases.

end of the century. Annual mean DOC concentrations decrease with increasing fraction HCP (Fig. 6F), but, depending on subsurface conditions, DOC flux increases when fraction coverage of HCP increases (Fig. 6C). Care should be taken when interpreting these results and projecting them onto a larger scale. Due to the high variability in real-world soil properties, (micro)topography and climate we stress that a broad-scale application of the model with spatially resolved parameterization is needed to assess the future change trajectory of DOC fluxes. Nonetheless, based on our model we can infer that in a warmer climate and more degraded (i.e., HCP dominated) system it is likely that deeper flow paths will result in a shift of the DOC export peak toward the late season.

3.2.1. Effects of temperature and precipitation change on annual fluxes

Catchment total DOC flux responds non-linearly to fraction HCP. Under current climate conditions, DOC flux decreases with increasing HCP (Fig. 6C, orange line) at a higher rate than under the late-century climate conditions (Fig. 6C, green line). Similarly, the effect of increased precipitation yields a decrease in DOC flux in an LCP-dominated catchment while it yields an increase in DOC flux in an HCP-dominated catchment (Fig. 6B). The impact of temperature (decrease of DOC flux with increased temperature) is biggest on LCP-dominated catchments, while HCP-dominated catchments show less decrease in total DOC flux with increased temperature (Fig. 6B). The rate at which total DOC flux changes with increasing fraction HCP varies between the forcing scenarios, i.e., each line has a different slope (Fig. 6A–C). From this we can infer that 1. LCP is more sensitive to climate change (i.e., the biggest shift in DOC flux in response to climate forcing), 2. under warmer and wetter climate we may expect the differences in DOC flux LCP and HCP to decrease (i.e., less steep slope of the lines in Fig. 6 A–C), and 3. under certain climate scenarios, the DOC flux associated with a shift to an HCP dominated catchment could hypothetically result in a net increase in DOC flux, when conditions of long residence time and sufficient soil water storage are met. Also, while HCP under current climate conditions is likely generating less DOC flux than LCP, our results show that total HCP flux will likely increase under future climate conditions (i.e., warmer and wetter) (Fig. 6A–C). Other studies (e.g., Liljedahl et al., 2012; Liljedahl et al., 2016) show deeper (and shorter) water storage in HCP and increasing drainage and runoff in catchments that transition from LCP to HCP-dominated terrain, consistent with our model results. The increase in runoff is likely caused by trapping of snow in HCP troughs, which causes the resulting meltwater to generate runoff relatively fast during spring melt. However, how the total water and DOC balance will play out in future climate comes down to an interplay of precipitation, temperature, consequent evaporation and the soil characteristics and ground ice dynamics unique to each catchment.

We acknowledge the limited accuracy of gridded reanalysis data (ERA5-Land in our case) for temperature and precipitation (e.g., Rapaić et al., 2015). We still used these data because they provide full spatial and temporal coverage across the arctic. However, for future use, we recommend using verified local datasets for site-specific modelling.

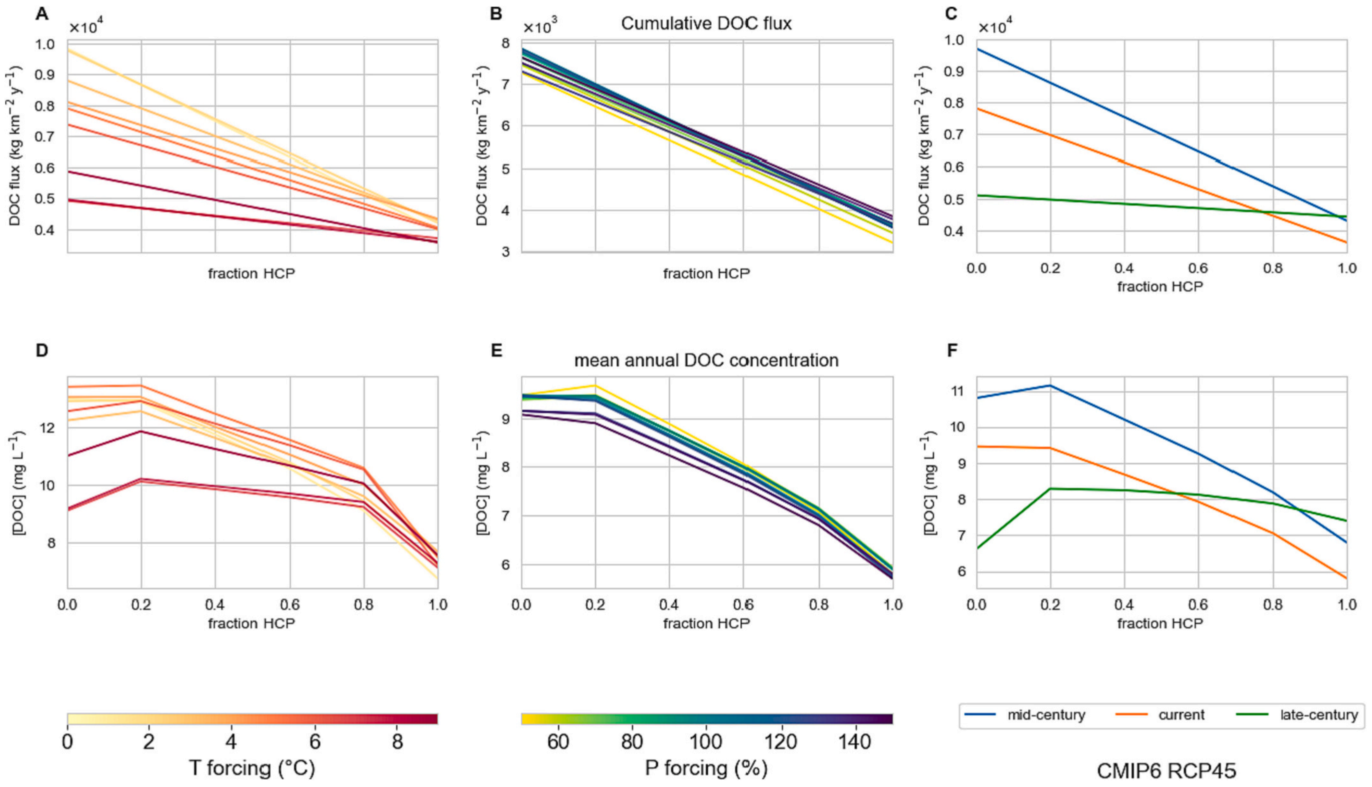

Fig. 6. Climate forcing scenarios from left to right: Temperature increase, precipitation shift and RCP45 scenario from CanESM2. The top row (A–C) shows the changes in annual catchment DOC export resulting from these climate forcings, the bottom row (D–F) shows the shift in annual mean DOC concentration.

3.3. Modelling constraints

Our modelling approach, which includes active layer evolution, gives valuable first-order insights into runoff and DOC dynamics in HCP and LCP systems, and a combined distribution on a catchment scale. We want to highlight a few processes that we have not considered in this version that may affect simulated processes. Multi-layered soil storage, thermal and hydrological impacts of plants, and interaction with surface water were not included and therefore insulating properties and evaporative fluxes are likely underestimated. As a result, active layer depths were initially overestimated, yet we balanced this overestimation by introducing an insulation layer correction factor to the soil freeze-thaw module. Our model only produces DOC estimates coming from soil and surface runoff, and assuming that surface runoff has a very short residence time (1 d), leaching of carbon from, e.g., litter in ponding water is neglected. To further narrow down relative contributions of such sources of DOC within the system, these processes should be incorporated into the model. We considered the supply of DOC to be constant with a stable SOC source-stock and associated DOC-leaching controlled by temperature and time, as well as abundant SOC that is homogeneously distributed in the soil. This assumption is based on the relatively shallow active layers and the high bulk SOC contents found in IWP systems. By incorporating a 'water age' component for the soil storage water we allow for temporal accumulation of DOC during periods of low throughflow and 'flushing' during periods of high throughflow. We acknowledge that layers of higher and lower SOC content exist in the soil and that e.g., presence of reducible iron in the soil may influence DOC production, but incorporating these processes was beyond the scope of this project. At the same time, longitudinal losses and degradation of DOC are also not incorporated in this model. Also, more field data may be needed to validate the model setup. In a time where large data-processing capacity keeps expanding, we see that a terrain-type-based conceptual modelling approach to quantifying catchment fluxes is a valuable tool and suited to go hand-in-hand with large-scale high-resolution mapping of permafrost terrain using machine learning techniques (e.g., Li et al., 2022).

4. Conclusion

In a warmer and wetter climate, seasonal active layers will grow deeper and persist longer. This leads to increased duration of the groundwater flow season. Initially, increased snowfall may result in bigger snowmelt peaks during the freshet, IWP terrain is likely to degrade significantly turning LCP-dominated catchments into HCP-dominated catchments. This is likely to result in a shift in the timing and magnitude of the early season peak. In this study, we present a first-order conceptual modelling approach to estimate runoff and DOC flux from low and high-centered polygons. We tested the model using field-based runoff, DOC concentration, stock, and flux. Finally, we ran climate sensitivity analysis for both ice wedge polygon types to temperature increase, precipitation increase, and a full RCP45 climate scenario produced by CanESM2. Our main findings are:

- Runoff from HCP dominates during the snowmelt (early) season in the form of surface runoff, while LCP dominates the runoff during the rest of the thawing season mostly through sub-surface flow.
- While water storage in LCP is generally larger and the residence time of water is often longer than in HCP, LCP is responsible for a relatively large proportion of runoff and annual DOC flux from a catchment with a 72–28 % HCP-LCP distribution.
- Our model indicates that, in a warmer and wetter climate, DOC concentrations remain largely unchanged throughout the year. However, the longer flow season causes the annual DOC flux to increase. This increase is modulated by specific soil conditions as more IWP terrain transitions into HCP and flow paths will run deeper. More field measurements and experiments are needed to refine the DOC-runoff coupling, especially for HCP systems. Residence time plays an important role for the exported DOC concentration,

however how the residence time will change with deepening active layers and shift to more well drained HCP systems is dependent on complex soil-water interactions that vary spatially. The direction of shifts in DOC flux therefore is place dependent.
- Based on a comparison with the catchment-specific DOC stock of the soil porewater, our model suggests that HCP systems are more well-drained, leading to a shorter residence time of soil DOC.
- The utility of a binary terrain type-based conceptual hydrological model to simulate runoff behavior and DOC fluxes in IWP terrain is demonstrated. This approach is fast, easily adaptable, and scalable and proves it can play a role in better quantification of current and future water and carbon budgets in permafrost regions. Additionally, our model provides a physical hypothesis that can be used to further quantify and refine our understanding of hydrology and DOC export of arctic ice-wedge polygon catchments.

5. Code availability

Our model code will be made available on request, by contacting the first author.

CRediT authorship contribution statement

Niek Jesse Speetjens: Data curation, Formal analysis, Investigation, Methodology, Software, Validation, Visualization, Writing – original draft, Writing – review & editing. **Wouter R. Berghuijs:** Conceptualization, Formal analysis, Investigation, Methodology, Software, Supervision, Writing – original draft, Writing – review & editing. **Julia Wagner:** Data curation, Methodology, Validation, Visualization. **Jorien E. Vonk:** Funding acquisition, Project administration, Resources, Supervision, Writing – review & editing.

Declaration of competing interest

The authors declare no competing interests.

Data availability

Data will be made available on request.

Acknowledgements

We would like to thank Moritz Langer and Sebastian Westermann for sharing their insights into modelling of ground freeze-thaw cycles.

Financial support

This research has been supported by Horizon 2020 (Nunataryuk; grant agreement no. 773421).

Appendix A. Supplementary data

Supplementary data to this article can be found online at https://doi.org/10.1016/j.scitotenv.2024.170931.

References

Andresen, C.G., Lawrence, D.M., Wilson, C.J., David McGuire, A., Koven, C., Schaefer, K., Jafarov, E., Peng, S., Chen, X., Gouttevin, I., Burke, E., Chadburn, S., Ji, D., Chen, G., Hayes, D., Zhang, W., 2020. Soil moisture and hydrology projections of the permafrost region-a model intercomparison. Cryosphere 14, 445–459. https://doi.org/10.5194/TC-14-445-2020.

Bartsch, A., Widhalm, B., Kuhry, P., Hugelius, G., Palmtag, J., Benjamin Siewert, M., 2016. Can C-band synthetic aperture radar be used to estimate soil organic carbon storage in tundra? Biogeosciences 13. https://doi.org/10.5194/bg-13-5453-2016.

Beckebanze, L., Runkle, B.R.K., Walz, J., Wille, C., Holl, D., Helbig, M., Boike, J., Sachs, T., Kutzbach, L., 2022. Lateral carbon export has low impact on the net ecosystem carbon balance of a polygonal tundra catchment. Biogeosciences 19. https://doi.org/10.5194/bg-19-3863-2022.

Bintanja, R., Andry, O., 2017. Towards a rain-dominated Arctic. Nat. Clim. Chang. 7 https://doi.org/10.1038/nclimate3240.

Blaschke, T., 2010. Object based image analysis for remote sensing. ISPRS J. Photogramm. Remote Sens. 65, 2–16. https://doi.org/10.1016/j.isprsjprs.2009.06.004.

Breiman, L., 2001. Random forests. Mach. Learn. 45, 5–32. https://doi.org/10.1023/A:1010933404324/METRICS.

Burn, C.R., 1997. Cryostratigraphy, paleogeography, and climate change during the early Holocene warm interval, western Arctic coast, Canada. Can. J. Earth Sci. 34 https://doi.org/10.1139/e17-076.

Coch, C., Ramage, J.L., Lamoureux, S.F., Meyer, H., Knoblauch, C., Lantuit, H., 2020. Spatial variability of dissolved organic carbon, solutes, and suspended sediment in disturbed low Arctic coastal watersheds. J. Geophys. Res. Biogeo. https://doi.org/10.1029/2019JG005505.

Conrad, O., Bechtel, B., Bock, M., Dietrich, H., Fischer, E., Gerlitz, L., Wehberg, J., Wichmann, V., Böhner, J., 2015. System for automated geoscientific analyses (SAGA) v. 2.1.4 system for automated geoscientific analyses (SAGA) v. 2.1.4 system for automated geoscientific analyses (SAGA) v. 2.1.4, Geosci. Model dev. Discuss 8, 2271–2312. https://doi.org/10.5194/gmdd-8-2271-2015.

Copernicus Climate Change Service, Climate Data Store, 2019. CORDEX regional climate model data on single levels. Copernicus Climate Change Service (C3S) Climate Data Store (CDS). https://doi.org/10.24381/cds.bc91edc3 (Accessed on 14-Mar-2023).

de Bruin, J.G.H., Bense, V.F., van der Ploeg, M.J., 2021. Inferring permafrost active layer thermal properties from numerical model optimization. Geophys. Res. Lett. 48 (16), e2021GL093306 https://doi.org/10.1029/2021GL093306.

Feng, D., Gleason, C.J., Lin, P., Yang, X., Pan, M., Ishitsuka, Y., 2021. Recent changes to Arctic river discharge. Nat. Commun. 12 https://doi.org/10.1038/s41467-021-27228-1.

Fenicia, F., Kavetski, D., Savenije, H.H., 2011. G.: elements of a flexible approach for conceptual hydrological modeling: 1. Motivation and theoretical development. Water Resour. Res. 47 https://doi.org/10.1029/2010WR010174.

Fritz, M., Wetterich, S., Schirrmeister, L., Meyer, H., Lantuit, H., Preusser, F., Pollard, W. H., 2012. Eastern Beringia and beyond: late Wisconsinan and Holocene landscape dynamics along the Yukon coastal plain, Canada, Palaeogeography, Palaeoclimatology. Palaeoecology. https://doi.org/10.1016/j.palaeo.2011.12.015.

Gisnås, K., Westermann, S., Vikhamar Schuler, T., Melvold, K., Etzelmüller, B., 2016. Small-scale variation of snow in a regional permafrost model. Cryosphere 10. https://doi.org/10.5194/tc-10-1201-2016.

Gisnås, K., Etzelmüller, B., Lussana, C., Hjort, J., Sannel, A.B.K., Isaksen, K., Westermann, S., Kuhry, P., Christiansen, H.H., Frampton, A., Åkerman, J., 2017. Permafrost map for Norway, Sweden and Finland. Permafr. Periglac. Process. 28 (2), 359–378. https://doi.org/10.1002/PPP.1922.

Hamon, W.R., 1961. Estimating Potential Evapotranspiration. J. Hydraul. Div. 87, 107–120. https://doi.org/10.1061/JYCEAJ.0000599.

Harp, D., Zlotnik, V., Abolt, C., Newman, B., Atchley, A., Jafarov, E., Wilson, C., 2020. New insights into the drainage of inundated Arctic polygonal tundra using fundamental hydrologic principles. Cryosphere Discuss. https://doi.org/10.5194/tc-2020-100.

Helbig, M., Boike, J., Langer, M., Schreiber, P., Runkle, B.R.K., Kutzbach, L., 2013. Spatial and seasonal variability of polygonal tundra water balance: Lena River Delta, northern Siberia (Russia). Hydrgeol. J. 21, 133–147. https://doi.org/10.1007/s10040-012-0933-4.

Hill, D.F., Burakowski, E.A., Crumley, R.L., Keon, J., Michelle, Hu, J., Arendt, A. A., Wikstrom Jones, K., and Wolken, G. J., 2019. Converting snow depth to snow water equivalent using climatological variables. Cryosphere 13. https://doi.org/10.5194/tc-13-1767-2019.

Hillel, D., 2013. Introduction to Soil Physics. https://doi.org/10.1016/C2009-0-03052-9.

Hock, R., 2003. Temperature index melt modelling in mountain areas. J. Hydrol. 282 https://doi.org/10.1016/S0022-1694(03)00257-9.

Hugelius, G., Strauss, J. (orcid:0000000346784982), Zubrzycki, S. (orcid:0000000263989173), Harden, J. W., Schuur, E. a. G., Ping, C.-L., Schirrmeister, L., Grosse, G., Michaelson, G. J., Koven, C. D., O'Donnell, J. A., Elberling, B., Mishra, U., Camill, P., Yu, Z., Palmtag, J., and Kuhry, P.: Estimated stocks of circumpolar permafrost carbon with quantified uncertainty ranges and identified data gaps, Biogeosciences, 11, doi:https://doi.org/10.5194/bg-11-6573-2014, 2014.

Jafarov, E.E., Svyatsky, D., Newman, B., Harp, D., Moulton, D., Wilson, C., 2022. The importance of freeze-thaw cycles for lateral tracer transport in ice-wedge polygons. Cryosphere 16, 851–862. https://doi.org/10.5194/TC-16-851-2022.

Jepsen, S.M., Harmon, T.C., Sadro, S., Reid, B., Chandra, S., 2019. Water residence time (age) and flow path exert synchronous effects on annual characteristics of dissolved organic carbon in terrestrial runoff. Sci. Total Environ. 656 https://doi.org/10.1016/j.scitotenv.2018.11.392.

Jones, E.L., Hodson, A.J., Redeker, K.R., Christiansen, H.H., Thornton, S.F., Rogers, J., 2023. Biogeochemistry of low- and high-centered ice-wedge polygons in wetlands in Svalbard. Permafr. Periglac. Process. 34 (3), 359–369. https://doi.org/10.1002/PPP.2192.

Kanevskiy, M., Shur, Y., Jorgenson, T., Brown, D.R.N., Moskalenko, N., Brown, J., Walker, D.A., Raynolds, M.K., Buchhorn, M., 2017. Degradation and stabilization of ice wedges: implications for assessing risk of thermokarst in northern Alaska. Geomorphology 297. https://doi.org/10.1016/j.geomorph.2017.09.001.

Karjalainen, O., Luoto, M., Aalto, J., Etzelmüller, B., Grosse, G., Jones, B.M., Lilleøren, K. S., Hjort, J., 2020. High potential for loss of permafrost landforms in a changing climate. Environ. Res. Lett. 15 https://doi.org/10.1088/1748-9326/abafd5.

Koch, J.C., Jorgenson, M.T., Wickland, K.P., Kanevskiy, M., Striegl, R., 2018. Ice wedge degradation and stabilization impact water budgets and nutrient cycling in arctic trough ponds. J. Geophys. Res. Biogeosci. https://doi.org/10.1029/2018JG004528.

Kokelj, S.V., Smith, C.A.S., Burn, C.R., 2002. Physical and chemical characteristics of the active layer and permafrost, Herschel Island, western Arctic coast, Canada. Permafr. Periglac. Process. 13, 171–185. https://doi.org/10.1002/ppp.417.

Kursa, M.B., Rudnicki, W.R., 2010. Feature selection with the boruta package. J. Stat. Softw. 36 https://doi.org/10.18637/jss.v036.i11.

Kurylyk, B.L., Hayashi, M., 2016. Improved Stefan equation correction factors to accommodate sensible heat storage during soil freezing or thawing. Permafrost and Periglacial Processes 27. https://doi.org/10.1002/ppp.1865.

Li, G., Zhang, M., Pei, W., Melnikov, A., Khristoforov, I., Li, R., Yu, F., 2022. Changes in permafrost extent and active layer thickness in the northern hemisphere from 1969 to 2018. Sci. Total Environ. 804, 150182 https://doi.org/10.1016/J.SCITOTENV.2021.150182.

Liaw, A., Wiener, M., 2002. Classification and Regression by randomForest, 2.

Liljedahl, A. K., Hinzman, L. D., and Schulla, J.: Ice-wedge polygon type controls low-gradient watershed-scale hydrology, in: Proceedings of the Tenth International Conference on Permafrost (Vol. 1), Salekhard, Russia, 231–236, 2012.

Liljedahl, A.K., Boike, J., Daanen, R.P., Fedorov, A.N., Frost, G.V., Grosse, G., Hinzman, L.D., Iijma, Y., Jorgenson, J.C., Matveyeva, N., Necsoiu, M., Raynolds, M. K., Romanovsky, V.E., Schulla, J., Tape, K.D., Walker, D.A., Wilson, C.J., Yabuki, H., Zona, D., 2016. Pan-Arctic ice-wedge degradation in warming permafrost and its influence on tundra hydrology. Nat. Geosci. 9, 312–318. https://doi.org/10.1038/ngeo2674.

McCrystall, M.R., Stroeve, J., Serreze, M., Forbes, B.C., Screen, J.A., 2021. New climate models reveal faster and larger increases in Arctic precipitation than previously projected. Nat. Commun. 12 https://doi.org/10.1038/s41467-021-27031-y.

Mishra, U., Drewniak, B., Jastrow, J.D., Matamala, R.M., Vitharana, U.W.A., 2017. Spatial representation of organic carbon and active-layer thickness of high latitude soils in CMIP5 earth system models. Geoderma 300. https://doi.org/10.1016/j.geoderma.2016.04.017.

Mishra, U., Hugelius, G., Shelef, E., Yang, Y., Strauss, J., Lupachev, A., Harden, J.W., Jastrow, J.D., Ping, C.L., Riley, W.J., Schuur, E.A.G., Matamala, R., Siewert, M., Nave, L.E., Koven, C.D., Fuchs, M., Palmtag, J., Kuhry, P., Treat, C.C., Zubrzycki, S., Hoffman, F.M., Elberling, B., Camill, P., Veremeeva, A., Orr, A., 2021. Spatial heterogeneity and environmental predictors of permafrost region soil organic carbon stocks. Sci. Adv. 7 https://doi.org/10.1126/sciadv.aaz5236.

Mohammed, A.A., Guimond, J.A., Bense, V.F., Jamieson, R.C., McKenzie, J.M., Kurylyk, B.L., 2022. Mobilization of subsurface carbon pools driven by permafrost thaw and reactivation of groundwater flow: a virtual experiment. Environ. Res. Lett. 17 https://doi.org/10.1088/1748-9326/aca701.

Moss, R.H., Edmonds, J.A., Hibbard, K.A., Manning, M.R., Rose, S.K., Van Vuuren, D.P., Carter, T.R., Emori, S., Kainuma, M., Kram, T., Meehl, G.A., Mitchell, J.F.B., Nakicenovic, N., Riahi, K., Smith, S.J., Stouffer, R.J., Thomson, A.M., Weyant, J.P., Wilbanks, T.J., 2010. The next generation of scenarios for climate change research and assessment. Nature 463. https://doi.org/10.1038/nature08823.

Muñoz-Sabater, J., Dutra, E., Agustí-Panareda, A., Albergel, C., Arduini, G., Balsamo, G., Boussetta, S., Choulga, M., Harrigan, S., Hersbach, H., Martens, B., Miralles, D.G., Piles, M., Rodríguez-Fernández, N.J., Zsoter, E., Buontempo, C., Thépaut, J.N., 2021. ERA5-land: A state-of-the-art global reanalysis dataset for land applications. Earth System Science Data 13. https://doi.org/10.5194/essd-13-4349-2021.

Nitzbon, J., Langer, M., Westermann, S., Martin, L., Aas, K.S., Boike, J., 2019. Pathways of ice-wedge degradation in polygonal tundra under different hydrological conditions. Cryosphere 13 (4). https://doi.org/10.5194/tc-13-1089-2019.

Nitzbon, J., Langer, M., Martin, L.C.P., Westermann, S., Schneider Von Deimling, T., Boike, J., 2021. Effects of multi-scale heterogeneity on the simulated evolution of ice-rich permafrost lowlands under a warming climate. Cryosphere 15, 1399–1422. https://doi.org/10.5194/TC-15-1399-2021.

Olefeldt, D., Goswami, S., Grosse, G., Hayes, D., Hugelius, G., Kuhry, P., Mcguire, A.D., Romanovsky, V.E., Sannel, A.B.K., Schuur, E.A.G., Turetsky, M.R., 2016. Circumpolar distribution and carbon storage of thermokarst landscapes. Nat. Commun. 7 https://doi.org/10.1038/ncomms13043.

Poggio, L., De Sousa, L.M., Batjes, N.H., Heuvelink, G.B.M., Kempen, B., Ribeiro, E., Rossiter, D., 2021. SoilGrids 2.0: producing soil information for the globe with quantified spatial uncertainty. SOIL 7. https://doi.org/10.5194/soil-7-217-2021.

R Core Team, 2021. R: A Language and Environment for Statistical Computing. R Foundation for Statistical Computing, Vienna, Austria. https://www.R-project.org/.

Rantanen, M., Karpechko, A.Y., Lipponen, A., Nordling, K., Hyvärinen, O., Ruosteenoja, K., Vihma, T., Laaksonen, A., 2022. The Arctic has warmed nearly four times faster than the globe since 1979. Communications Earth and Environment 3. https://doi.org/10.1038/s43247-022-00498-3.

Rapaić, M., Brown, R., Markovic, M., Chaumont, D., Rapai˙c, M., 2015. R.: an evaluation of temperature and precipitation surface-based and reanalysis datasets for the Canadian Arctic. Atmosphere-Ocean 53, 283–303. https://doi.org/10.1080/07055900.2015.1045825.

Schuur, E.A.G., Bockheim, J., Canadell, J.G., Euskirchen, E., Field, C.B., Goryachkin, S. V., Hagemann, S., Kuhry, P., Lafleur, P.M., Lee, H., Mazhitova, G., Nelson, F.E., Rinke, A., Romanovsky, V.E., Shiklomanov, N., Tarnocai, C., Venevsky, S., Vogel, J. G., Zimov, S.A., 2008. Vulnerability of permafrost carbon to climate change: implications for the global carbon cycle. BioScience 58. https://doi.org/10.1641/B580807.

Speetjens, N.J., Tanski, G., Martin, V., Wagner, J., Richter, A., Hugelius, G., Boucher, C., Lodi, R., Knoblauch, C., Koch, B.P., Wünsch, U., Lantuit, H., Vonk, J.E., 2022. Dissolved organic matter characterization in soils and streams in a small coastal low-Arctic catchment. Biogeosciences 19. https://doi.org/10.5194/bg-19-3073-2022.

Speetjens, N.J., Hugelius, G., Gumbricht, T., Lantuit, H., Berghuijs, W.R., Pika, P.A., Poste, A., Vonk, J.E., 2023. The pan-Arctic catchment database (ARCADE). Earth System Science Data 15, 541–554. https://doi.org/10.5194/ESSD-15-541-2023.

Vonk, J.E., Tank, S.E., Walvoord, M.A., 2019. Integrating hydrology and biogeochemistry across frozen landscapes. Nat. Commun. https://doi.org/10.1038/s41467-019-13361-5.

Vonk, J.E., Speetjens, N.J., Poste, A.E., 2023. Small watersheds may play a disproportionate role in arctic land-ocean fluxes. Nat. Commun. 14 (1), 3442. https://doi.org/10.1038/s41467-023-39209-7.

Vremec, M., Collenteur, R., 2021. PyEt - a Python Package to Estimate Potential and Reference Evapotranspiration. EGU21. https://doi.org/10.5194/EGUSPHERE-EGU21-15008.

Wagner, J., Martin, V., Speetjens, N.J., A'Campo, W., Durstewitz, L., Lodi, R., Fritz, M., Tanski, G., Vonk, J.E., Richter, A., Bartsch, A., Lantuit, H., Hugelius, G., 2023. High resolution mapping shows differences in soil carbon and nitrogen stocks in areas of varying landscape history in Canadian lowland tundra. Geoderma 438, 116652. https://doi.org/10.1016/J.GEODERMA.2023.116652.

Wales, N.A., Gomez-Velez, J.D., Newman, B.D., Wilson, C.J., Dafflon, B., Kneafsey, T.J., Soom, F., Wullschleger, S.D., 2020. Understanding the relative importance of vertical and horizontal flow in ice-wedge polygons. Hydrol. Earth Syst. Sci. 24 https://doi.org/10.5194/hess-24-1109-2020.

Witharana, C., Bhuiyan, M. A. E., Liljedahl, A. K., Kanevskiy, M., Jorgenson, T., Jones, B. M., Daanen, R., Epstein, H. E., Griffin, C. G., Kent, K., and Ward Jones, M. K.: An Object-Based Approach for Mapping Tundra Ice-Wedge Polygon Troughs from Very High Spatial Resolution Optical Satellite Imagery, Remote Sensing 2021, Vol. 13, Page 558, 13, 558, doi:https://doi.org/10.3390/RS13040558, 2021.

Zlotnik, V.A., Harp, D.R., Jafarov, E.E., Abolt, C.J., 2020. A model of ice wedge polygon drainage in changing arctic terrain. Water (Switzerland) 12. https://doi.org/10.3390/w12123376.